Article

Potent *E. coli* M-17 Growth Inhibition by Ultrasonically Complexed Acetylsalicylic Acid−ZnO−Graphene Oxide Nanoparticles

Anastasia Tkach, Aliaksandr Burko, Hanna Bandarenka, Tatyana Khrustaleva, Dmitry Zhigulin, Ljudmila Tabulina, Vladimir Labunov, Kateřina Veltruská, Vladimír Matolín, and Darya Radziuk*

Read Online

ACCESS | Metrics & More | Article Recommendations | Supporting Information

ABSTRACT: A single-step ultrasonic method (20 kHz) is demonstrated for the complexation of acetylsalicylic acid (ASA)−ZnO−graphene oxide (GO) nanoparticles with an average size of <70 nm in aqueous solution. ASA−ZnO−GO more efficiently inhibits the growth of probiotic *Escherichia coli* strain M-17 and exhibits enhanced antioxidant properties than free ASA and ASA−ZnO in neutralization of hydroxyl radicals in the electro-Fenton process. This improved function of ASA in the ASA−ZnO−GO can be attributed to the well-defined cone-shaped morphology, the surface structure containing hydroxyl and carboxylate groups of ZnO−GO nanoparticles, which facilitated the complexation with ASA.
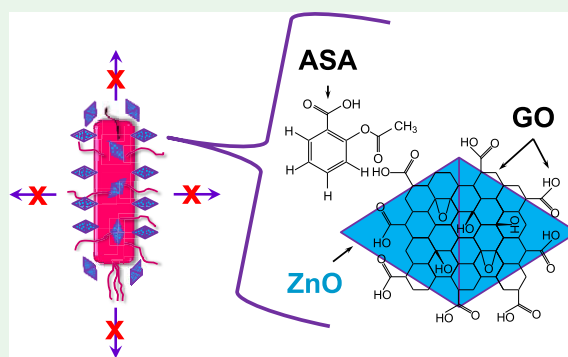
1. INTRODUCTION

Probiotic *Escherichia coli* (e.g., *E. coli* Nissle 1917,[1] *E. coli* clade B2 commensal,[2] or *E. coli* M-17[3]) are the first bacteria to colonize the gastrointestinal tract of humans upon birth and act as a barrier against pathogens, protecting the host from infections. Unlike abiotic therapeutics, probiotic *E. coli* can replicate in the gut, alleviate inflammation, and strengthen the host innate immune functions via site-specific expression of biomolecules. For this reason, probiotic *E. coli* are encouraged by the European Union and World Health Organization (CDC 2014) because these nonpathogenic bacteria are live microorganisms, which at appropriate amounts maintain the health of the host.[4]

E. coli M-17 is a novel probiotic, non-spore-forming Gram-negative rod of the serotype O₂ with flagellum antigen H type 41 and a facultative anaerobic bacillus, and is oxidase-negative and catalase-positive.[3] *E. coli* M-17 is the main component of probiotics to treat rotavirus infection.[5] Many studies have been performed on *E. coli* M-17 bacteria to examine the growth of their pure culture or as a pair with probiotic *E. coli* LEGM-18,[6] to identify their growth stimulators[7] and to find out the healing effects in patients with inflammation of the small bowel.[8] However, at present, little knowledge exists about the growth modulation of probiotic *E. coli* M-17 bacteria with nonsteroidal anti-inflammatory drugs (NSAIDs), and their molecular interaction is not understood.

So far, NSAIDs have been applied in co-treatment of bacterial infections, and among them, acetylsalicylic acid (ASA) has shown a significant inhibition effect of bacterial

clinical isolates.[9] It was demonstrated that the *E. coli* growth inhibition by ASA depends on the bacterial strain type, modification, and concentration of the drug as a result of upregulation of certain genes, and protein damage. ASA causes downregulation of genes in bacteria, inhibits quorum sensing, reduces virulence and toxins, and protects human melanocytes against H₂O₂-induced oxidative stress.[10]

Contact-dependent growth inhibition is one of competitive mechanisms, which have been identified in probiotic *E. coli* bacteria.[11] The probiotic *E. coli*-mediated growth inhibition involves a Zn²⁺-dependent enzymatic process, resulting in degradation of the target-cell genomic DNA. Zinc supplementation can be used in prophylaxis to reduce diarrhea morbidity or as a treatment to shorten the duration of symptoms, and ZnO can protect the cultured human enterocytes from the damage by inhibiting the adhesion of pathogenic bacteria.

It was reported that small ZnO nanoparticles (NPs) (<100 nm) exhibit shape-dependent biomimetic inhibition of enzyme and antibacterial activity,[12] and have been used in the treatment for oral biofilms[13] and bacterial infections.[14] Overall, ZnO is considered biocompatible and biosafe as approved by
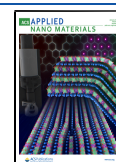
U.S. Food and Drug Administration (FDA).[15] Although the modes of antibacterial action of ZnO NPs are not entirely understood, it has been observed that the bacterial growth inhibition can be increased if smaller NPs are used (6.8 nm size; ~99.8%) and their concentration is below 100 μg/mL. Three possible mechanisms have been proposed explaining the bacterial growth inhibition by ZnO NPs: (1) bacterial membrane disruption caused by the active surface area of NPs and their concentration; (2) generation of oxidative stress by the formation of reactive oxygen species (ROS); and (3) toxicity caused by the release of free Zn^{2+} ions.

The active surface area and stability of NPs can be modulated by the deposition, precipitation, or adsorption of ZnO on graphene oxide (GO).[16] GO is biocompatible and its interaction with *E. coli* can be controlled by the oxidation degree (i.e., amount of oxygen functional groups), C radical density, and orientation of nanosheets.[17] In addition, the extended two-dimensional (2D) surface of GO can serve as a storage for concentration-dependent released Zn^{2+} ions. Deposition of ZnO NPs on GO significantly reduces the minimum inhibitory concentration (MIC) of *E. coli* (~7 μg/mL) as GO cuts the bacterial membrane. Moreover, ZnO–GO NPs can enable a long-term antibacterial activity without affecting the viability of the HeLa cells. At a higher concentration, these NPs can form complexes with pathogens, leading to either inhibition or enhancement of bacterial growth in a surface potential-dependent manner.

Many methods such as hydrothermal,[18] solvothermal,[19] spray pyrolysis,[20] microwave-assisted,[21] and sonochemical[22] have been introduced to produce ZnO NPs with various carbon-containing structures (e.g., carbon dot-ZnO, GO-Zn, or spindle-like ZnO–GO) for various biological applications.[23] In particular, ZnO NPs have been used for encapsulation of anticancer therapeutics 9-aminoacridine hydrochloride hydrate,[24] isotretinoin,[25] doxorubicin,[26] paclitaxel,[27] plant flavonols (quercetin,[28] propolis extracts)[29] into ZnO nanoparticles or quantum dots. Only few studies have been performed on the integration of pharmaceutical compounds such as gentamicin[30] or doxorubicin[31] onto ZnO–GO nanoparticles to be used as nanocarriers for drug delivery applications. Most of mesoporous ZnO scaffolds showed controlled drug loading efficiency and faster in vitro release kinetics, while GO facilitated enhanced bioactivity at the contact with live cells. Distinct from these studies, we have recently proposed a new concept based on the functionalization of pristine drugs through complexation with preformed metal–metal or metal–oxide–graphene nanoparticles by ultrasound. Instead of loading or encapsulation of drugs, we have demonstrated the functionalization of pristine NSAIDs such as ketorolac, ASA, and diclofenac through the sonochemical complexation with preformed Cu/Fe–GO,[32] Fe_3O_4–GO,[33] or CuO–GO[34] nanoparticles with improved pH-dependent hydrophilicity properties. Copper, copper/iron, and iron–graphene–ketorolac nanoparticles acquired higher surface-active area, which facilitated the drug disintegration at a slower rate from copper/iron–graphene–ketorolac at increased pH, but at a faster rate from iron–graphene–ketorolac nanoparticles starting from acidic conditions. Superparamagnetic Fe_3O_4–graphene–ketorolac nanoparticles enabled drug extraction at pHs 1 and 5 being controlled by the H-bond formation and Fe_3O_4, and at pH 8—predominantly via interaction with GO. Recently we have demonstrated that poly(vinyl alcohol) can enhance acetylation of ascorbic acid in

superparamagnetic-GO NPs ultrasonically complexed with ASA in relation to free unmodified drug or uncoated ASA–Fe_3O_4–GO NPs due to enhanced electron density through the presence of magnetite and GO, and specific binding of polymer with drug and ascorbic acid.[35] The surface composition and electronic molecular structure of ASA–GO-coated CuO and diclofenac-GO-coated CuO nanoparticles can be modified at pH from 1 to 8 through the specific interactions involving Cu–O, C–H, and H-bond formation with the carboxylic and carbonyl groups of ASA, diclofenac, and GO.

In this study, we demonstrate a new single-step ultrasonic method (20 kHz) for the complexation of free ASA with preformed ZnO–GO NPs without any surface-active additives in aqueous medium. In our work both ZnO and GO are chosen because they satisfy the FDA rules and can enhance the electron density of ASA–ZnO–GO NPs. Here, the antibacterial activity of ASA–ZnO–GO NPs will be examined in interaction with the probiotic *E. coli* M-17. The antioxidant properties of these NPs will be studied in the electro-Fenton process as a model system. The complexation of ASA with ZnO and GO can be useful in the understanding of the drug–metal and drug–graphene interaction, activation of NSAIDs by metal ions and oxides, and the fundamental studies of the drug–enzyme mechanisms.

2. EXPERIMENTAL SECTION

2.1. Materials and Synthesis. Graphite with ca. 10–50 μm dispersion, ~68 nm crystallite size, composition C (95.0 ± 2.0 atom %) and O (4.0 ± 1.0 atom %), and ~1 atom % impurities (Ti, Ca, Mn) was donated by the State Transport Unitary Enterprise "Minsktrans" (the Republic of Belarus). $KMnO_4$, H_2SO_4, H_3PO_4, H_2O_2 (50%), HCl (35%), KOH (44%), KCl, NaOH, C_2H_5OH, C_3H_8O, $ZnSO_4·7H_2O$, and $Na_2HPO_4·7H_2O$ are of higher-grade purity being obtained from Belreachim JSC (the Republic of Belarus). $FeCl_2$ (98%) was purchased from Sigma-Aldrich GmbH. Pharmaceutics "Bioflor" containing live *E. coli* M-17 was purchased from Ferane, Inc. (the Republic of Belarus). A saline solution (0.9% NaCl) was obtained from OJSC Nesvizh Plant of Medical Preparations (the Republic of Belarus). Deionized water (DI; pH 5.5, specific conductivity 5 μS/cm) was prepared using a distillation apparatus, which has been set up in the laboratory "Integrated Micro- and Nanosystems" at the Belarusian State University of Informatics and Radioelectronics (the Republic of Belarus). GO was synthesized using the improved Hummers method[36] (more details are in the Supporting Information). Pristine NSAID—acetylsalicylic acid (ASA, 4.21 wt %) was purchased from Belmedpreparaty RUE (Minsk, the Republic of Belarus). Fine powder of ASA was produced by grinding 10 tablets with an agate mortar and a pestle. The aqueous solution of ASA was prepared by dissolving a powder of this drug in DI water (pH 5.5) under continuous stirring at a critical concentration of dissolution at room temperature according to the literature.[37] For experiments, NSAID aqueous solutions were filtered through a cellulose membrane filter (red line; pore size, 8–12 nm).

2.1.1. Sonochemical Formation of ZnO and ZnO–GO Nanoparticles. A horn-type ultrasonic disperser N.4-20 (20 kHz, 400 W) designed by Cavitation, Inc. (the Republic of Belarus) was used for the sonochemical synthesis of nanoparticles. The ultrasonic intensity of this device was calibrated using a method of calorimetry.[38]

Formation of ZnO nanoparticles: in a vessel of 30 mL DI water, 0.05 M $ZnSO_4$ was mixed with 30 mL of 0.125 M NaOH DI aqueous solution in a single addition under mechanical stirring and was heated at ≈90 °C in an air atmosphere for 30 min. Soon after, it was sonicated (18 W/cm^2) for 15 min in an air atmosphere and cooled down to room temperature. Then, the colloidal solution was triply rinsed with DI water (pH 5.5) at 6.7 g for 45 min and air-dried at 120 °C to obtain a powder.

Formation of ZnO−GO nanoparticles: prior to the synthesis, 27.5 mg of GO was exfoliated in 30 mL of DI water (pH 5.5) using ultrasound (10 W/cm^2) for 30 min in an ice-cooled vessel. The exfoliated GO was triply rinsed with DI water by centrifugation at 7.3g for 45 min and added with 2 mL of DI water (pH 5.5) followed by 3 min of sonication to obtain a homogeneous colloidal solution. A mixture of 0.05 M ZnSO$_4$ and 0.125 M NaOH in 60 mL of DI water was thermally treated at ≈90 °C under continuous mechanical stirring for 30 min. Then, it was added with 2 mL of exfoliated GO colloidal solution and sonicated for 15 min in an air atmosphere. Soon after, this colloidal solution was cooled down to room temperature and triply rinsed with DI water (pH 5.5) by centrifugation at 6.7g for 45 min and air-dried at 100 °C to obtain a powder.

2.1.2. Ultrasonic Formation of ASA−ZnO and ASA−ZnO−GO Nanoparticles. Ultrasonic functionalization of pristine ASA with ZnO nanoparticles: in a sealed vessel, 30 mg of sonochemically synthesized ZnO nanoparticles were added with 30 mL of DI water (pH 5.5) and mechanically stirred. After 15 min, it was added with 30 mg of ASA (in a powder form) and sonicated for 3 min at 18 W/cm^2 in an air atmosphere. Then, this colloidal solution was rinsed five times with DI water (pH 5.5) by centrifugation at 4.2g for 75 min and air-dried at 100 °C to obtain a powder. Control experiment of free ASA sample was performed by dissolving 30 mg of pristine ASA powder in 30 mL of DI water (pH 5.5) under mechanical stirring and heating ($T \approx 35$ °C) for 10 min in a sealed vessel followed by five times rinsing with DI water (pH 5.5) by centrifugation at 4.2g for 75 min and air-drying at 100 °C to obtain a powder.

Ultrasonic functionalization of pristine ASA with ZnO−GO nanoparticles: in a sealed vessel, 30 mg of sonochemically synthesized ZnO−GO nanoparticles were added with 30 mL of DI water (pH 5.5) and mechanically stirred for 15 min. Soon after, it was added with 30 mg of ASA (in a powder form) and sonicated for 3 min at 18 W/cm^2 and in an air atmosphere. Then, this colloidal solution was rinsed five times with DI water (pH 5.5) by centrifugation at 6.7g for 75 min and air-dried at 100 °C to obtain a powder.

2.1.3. E. coli Strain M-17 Bacteria Assessment in Aqueous Solutions of Free ASA, ASA−ZnO, and ASA−ZnO−GO Nanoparticles as Test Substances. A pharmaceutics Bioflor, being approved in 2010 by Ministry of Health of the Republic of Belarus, was used for the preparation of *E. coli* M-17 inoculums. Bioflor contains *E. coli* M-17 as an active substance in the amount of not less than 100×10^8 live cells at the moment of preparation and not less than 100×10^7 live cells at the end of the expiration date. In addition, Bioflor also contains ingredients such as 0.7 g of NaCl (State Pharmacopoeia II volume 2, p. 740), not more than 100 mL of DI water (State Pharmacopoeia II volume 2, p. 309) and 0.8 g of a mixture of vegetable extract (soy, dill, beet, peppermint, garlic, parsley, cabbage) and propolis (standard organization-OS-029). A suspension of Bioflor was diluted to 10^6 colony-forming units (CFU/mL) with saline (0.9% NaCl) solution and used as inoculum.

Fresh aqueous colloidal suspensions were prepared to avoid the undesired agglomeration. Overall, 50 μL of each test substance was added to the corresponding tubes with 1 mL of bacterial inoculums, which corresponded to the concentration of ASA 3.34 μmol/L in free ASA, 0.02 μmol/L in ASA−ZnO, and 2.68 μmol/L in ASA−ZnO−GO NPs. A positive control without antibacterial samples was included to evaluate the viability of the bacteria. Also, the same saline (with no microorganism but containing the same amount of antibacterial agents) was prepared and considered as a blank control. Then, all tubes were shaken followed by incubation at 37 °C for 30 min. Experiments were performed in duplicate. The *E. coli* M-17 growth inhibition was assessed by the colony-counting method, i.e., 100 μL aliquots from each tube were sampled and plated on nutrient Endo agar and incubated at 37 °C for 20 h. Then, the colonies were counted and their surface areas were calculated using the optical phase contrast microscope. The number of colonies and their surface area (μm^2) were expressed as the mean standard error (SE) and relative standard error (RSE %), standard deviation (SD), and relative standard deviation (RSD %).

2.2. Equipment and Analytical Methods. The synthesized materials and their interaction with *E. coli* M-17 were characterized using several methods: scanning electron microscopy (SEM) and energy-dispersive X-ray fluorescence (EDX), ζ-potential, X-ray powder diffraction (XRD), UV−visible absorption spectroscopy, Raman and surface-enhanced Raman scattering (SERS) spectroscopy, X-ray photoelectron spectroscopy (XPS), and optical phase contrast microscopy.

The morphology and elemental composition of sonochemically prepared NPs were analyzed and characterized by SEM (S-4800) Hitachi, Japan. The ζ-potential of aqueous colloidal solutions was measured using a Zetasizer Nano instrument from Malvern Instruments Ltd. and a prepared buffer solution (more details are in the Supporting Information). The ζ-potential (electrical charge) experiments were carried out on a diluted colloidal suspension. Each measurement was repeated several times being each for 10 s; the nanoparticle electrophoretic curves were obtained by averaging 10 measurements. The phase composition was determined using powder diffraction patterns recorded with an EMPYREAN diffractometer (PANalytical, the Netherlands) using Cu Kα radiation (Ni-filter) at 296 K. The UV−visible absorption spectra of colloidal solutions were recorded using a Cary-500 spectrophotometer (Varian, USA) in the wavelength range of 200−1100 nm. For measurements, aqueous solutions were placed in a quartz (SUPRASIL) cuvette Hellma Analytics 111-QS (Z600725) with a path length of 10 mm.

2.2.1. Electrochemical Measurements (Electro-Fenton Process). The electro-Fenton process, i.e., iron-catalyzed H$_2$O$_2$ decomposition, is one of the most used electrochemical oxidation reactions. This Fenton reaction is based on the electrochemical formation of hydroxyls and hydroxyl radicals through the process of hydrogen peroxide decomposition catalyzed by iron cations Fe^{2+}. In an experiment, 1 mM FeCl$_2$ (used as catalyst) in DI water and 20 mM Na$_2$HPO$_4$ (used as phosphate-buffered solution, pH 9) in DI water were mixed at a volume ratio of 1:1. This mixture was added with 2 mM H$_2$O$_2$ (50%) at a volume ratio of 1:1:1 or 1:1:2 to perform the electro-Fenton process in a final volume of 20 mL in a glass vessel equipped with a three-electrode system containing two custom graphite paper sheets with the geometrical size 43 ×17 mm and one Ag/AgCl electrode. A saturated stock 5 mol/L KCl aqueous solution was used as a supported electrolyte. Electrochemical measurements (cyclic voltammetry) were performed with the Metrohm Autolab potentiostat/galvanostat instrument operating with the Nova 1.11 software allowing data acquisition and their sophisticated analysis. In electrochemical experiments with NPs, fresh aqueous solutions of free ASA acidified by H$_2$SO$_4$ (98.08 wt %) to pH 3−4, ASA−ZnO and ASA−ZnO−GO were consequently added into the freshly preformed solution for the Fenton reaction in a volume of 1 mL in the total amount of 5−8 mL during the electrochemical process of 10 scans at a scan rate of 0.1 v/s in the applied voltage range of −0.5 to +1.2 V.

2.2.2. Raman and Surface-Enhanced Raman Spectroscopy (SERS). Raman and SERS spectra were recorded using a three-dimensional (3D) scanning laser confocal Raman microscope Confotec NR500 (SOL Instruments Ltd., the Republic of Belarus) at 633 nm excitation wavelength with a grating 600 gr/mm blazed at 600 nm. The Si wafer with the characteristic Raman line at 520 cm^{-1} was taken as a reference for calibration and basic alignment during integration time from 1 to 3 s. The SERS-measurements were performed with the silvered porous silicon (Ag/PS) substrates described elsewhere[39] to enhance Raman signals of molecular compounds. The SERS-active substrates were kept in each freshly prepared aqueous colloidal solution for 2 h and then taken out of glass vessels. Soon after, incubated SERS-active substrates were rinsed with DI water and air-dried. The acquired Raman and SERS spectra were corrected for the baseline and a background of the SERS-active substrates based on Ag/PS. A linearly polarized diode laser beam was focused through the objectives with 40× and 100× magnification for Raman and SERS spectra acquisition. The laser power (4 mW) was attenuated using neutral density filters with the following optical density (OD) values: 0.6 (25), 0.3 (50), and no filter (100).

2.2.3. X-ray Photoelectron Spectroscopy. An XPS spectrometer equipped with hemispherical electron energy analyzer and non-monochromatized X-ray Al Kα source with $h\nu$ = 1486.6 eV was employed to acquire XPS spectra of samples in ultrahigh vacuum (UHV) conditions. Original XPS spectra were corrected for a Shirley background and fitted by Gaussian−Lorentzian peak shape (red line) using the KolXPD 1.8.0 software developed by scientists in the Charles University, Faculty of Mathematics and Physics (Prague, Czech Republic) (https://www.kolibrik.net/kolxpd).

2.2.4. Optical Phase Contrast Microscopy. Samples of Petri dishes were examined for optical light phase contrast microscopy, by direct visualization of *E. coli* M-17 colonies. The surface area of grown bacterial colonies was analyzed via a high-speed camera connected to an optical light microscope (Planar MKI-2M) through taking photographs in real time and characterized by software imaging tool ScopeTek Photo 3.1.312 (×86) of individual colonies. Two main microscope objectives with the A/F (aperture/focus) 0.08/48 (yellow) and 0.5/6 (white) with the resolutions 936 pxl and 7290 pxl in 1 mm were used. Size distribution histogram: the standard statistical method in electron microscopy was applied to estimate the average size of NPs

$$\Gamma = \frac{\sum d_i n_i}{N} \qquad (1)$$

where Γ is the estimated average size (nm) of NPs, d_i is the average size of each cluster of NPs per surface area, n_i is the number of NPs in each cluster, and N is the total number of NPs.

$$S = \frac{1}{4}\pi d_i^2 n_i \qquad (2)$$

where S is the surface area of the projection of NPs in each cluster (nm^2). The estimated values of d_i (nm), n_i, S (nm^2), and Γ of the formed ZnO and ZnO−GO NPs are listed in Tables S1 and S2 in the Supporting Information. Crystallite size t of ZnO and ZnO−GO NPs was estimated using the Scherrer formula (eq 3) (XRD analysis) with the measured XRD patterns.

$$t = \frac{k\lambda}{\beta \cos \theta_B} \qquad (3)$$

where k is the constant depending on the crystallite shape (k = 0.89 for ZnO), λ is the X-ray wavelength (Cu Kα = 1.54 Å), β is the integral breadth or full width at half-maximum, and θ_B is the Bragg angle. The most intense diffraction reflexes at $2\theta_B$ = 36.22° for ZnO with β = 0.325 and $2\theta_B$ = 36.18° for ZnO−GO nanoparticles with β = 0.365 were used to calculate t values.

2.2.5. Quantitative Estimation of the "ASA:Starch" Ratio by Raman Spectroscopy. Laser Raman spectroscopy was used for quantitative estimation of starch in ASA samples by the intensity ratio method.[40] Distinct free ASA Raman peaks ∼548, ∼640, and ∼1606 cm^{-1}, and the characteristic starch Raman peak ∼478 cm^{-1} were examined. For calculation, the molecular weights of ASA ∼180.2 g/mol and of starch ∼692.7 g/mol of 30 mg of substance were used in our experiments. The concentration values C of starch (C_{starch} = 0.043 mM) and ASA (C_{ASA} = 0.167 mM) were estimated in our samples

$$C = \frac{W}{MW} \qquad (4)$$

where W is the weight and MW is the molecular weight of the substance.

$$\frac{I_{ASA}}{I_{starch}} = \frac{K_{ASA}}{K_{starch}} \cdot \frac{W_{ASA}}{W_{starch}} \text{ or } \frac{I_{ASA}}{I_{starch}} = \alpha \cdot \frac{W_{ASA}}{W_{starch}} \qquad (5)$$

where I_{ASA} and I_{starch} are the Raman scattering intensities, K_{ASA} and K_{starch} are the constants of ASA and starch Raman bands, respectively, which include the $G(\nu)$ factor and MW of a substance, and α is the coefficient representing the features of ASA, starch, and the spectrometer conditions being defined as the K_{ASA}/K_{starch} ratio.

3. RESULTS AND DISCUSSION

First, ZnO−GO NPs were synthesized by ultrasound (20 kHz) to enhance the electronic molecular structure and amphiphilicity of pristine ASA due to complexation with ZnO and GO (Scheme 1). For comparison, free ASA was also ultrasonically

Scheme 1. Modification of Live Probiotic *E. coli* M-17 with Ultrasonically Formed ASA−ZnO−GO NPs Results in Potent Bacteriostatic Effect in Contrast to Free ASA[a]
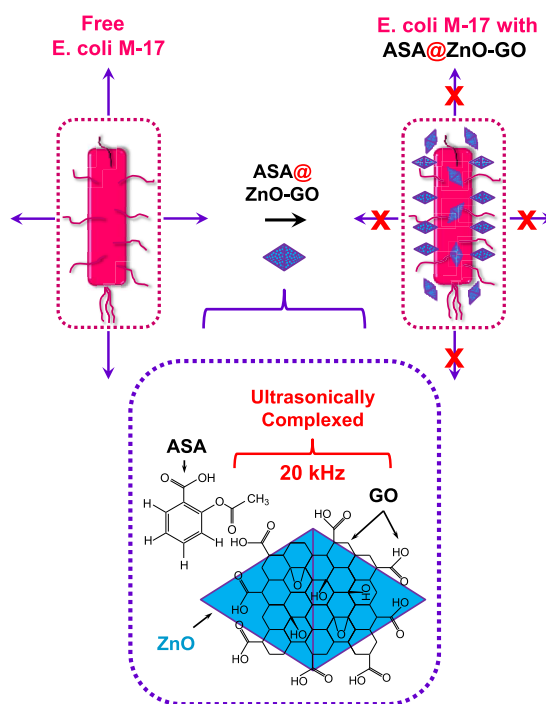
[a]Ultrasound (20 kHz) causes complexation of pristine ASA with sonochemically formed ZnO−GO, resulting in the formation of ASA−ZnO−GO NPs with properties inaccessible to unmodified ASA.

modified with preformed ZnO NPs. As a result, new potential pharmaceutical compounds such as ASA−ZnO and ASA−ZnO−GO NPs were formed. Second, the bacteriostatic effects of free ASA, ASA−ZnO, and ASA−ZnO−GO NPs were examined in experiments with live probiotic *E. coli* M-17 bacteria at a concentration of compounds, at which most of eukaryotic cells are still alive, important for *in vivo* studies and clinical applications.

3.1. Morphology and Structure of ZnO−GO Nanoparticles.
SEM images show synthesized ZnO−GO in comparison to ZnO NPs, revealing the irregular shape consisting of small aggregated crystallites with a nonuniform size distribution (Figure 1A,B). Most of ZnO NPs have a spherical shape and are grown into larger nanoparticles with random orientation. In contrast, formed ZnO−GO NPs have a cone-shaped morphology being composed of small crystallites. The powders of NPs have different colors: white, ZnO; gray, ZnO−GO (insets in Figure 1).

The final morphology and size of NPs depend on the mole ratio of precursors and the sequence of addition of aqueous solution of ZnSO$_4$ and NaOH during the thermal treatment at T < 100 °C.[41] At OH$^-$/Zn^{2+} mole ratio 2.5, smaller rounder particles with ZnO wurtzite structure are produced, indicating that the larger excess of OH$^-$ ions leads to a complete chemical reaction. When NaOH aqueous solution is added to the
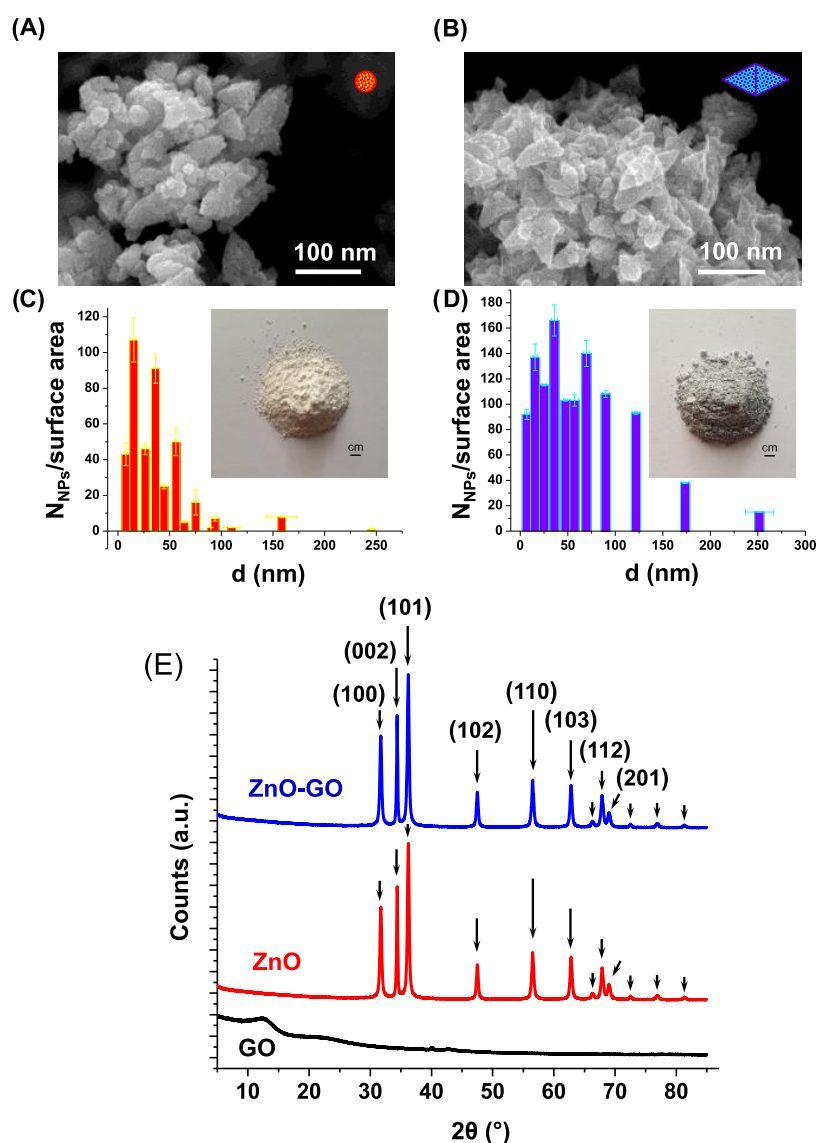
Figure 1. Representative SEM images of ultrasonically formed (A) ZnO and (B) ZnO−GO NPs. Size distribution histogram of (C) ZnO and (D) ZnO−GO NPs shows the number of NPs per surface area versus the size d (nm) being calculated using the standard statistical method in electron microscopy (more details in the Supporting Information). The two insets show the powders of formed NPs: white, ZnO; gray, ZnO−GO. The scale bar is 1 cm. (E) X-ray powder diffraction patterns of formed GO, ZnO, and ZnO−GO NPs reveal the amorphous structure of GO and the crystalline ZnO wurtzite phase. The color insets in the SEM images (A, B) illustrate the nucleation centers.

ZnSO$_4$ solution in a single addition (as in our experiments), the amount of hydroxide passes the stoichiometric ratio very rapidly and Zn−OH species are formed, followed by decomplexation and fast production of ZnO. The number of nucleation sites is more than sufficient, leading to the particle growth of small (<100 nm) round NPs. When ZnSO$_4$ aqueous solution is added to the NaOH solution in a single addition, the reaction rapidly proceeds from soluble zinc complex to formation of ZnO nuclei. Fewer nuclei are formed, leading to the production of larger cone-shaped NPs. NPs are synthesized through the formation of Zn−OH species, followed by their subsequent decomplexation via solubility and precipitation of ZnO. The solubility of zinc hydroxide species depends on the type of anions. In the case of ZnO−GO, OH$^−$, and COO$^−$ anions are formed at pH 5.5. At this pH value, both solid Zn(OH)$_2$ and ZnO can be produced. In general, the decomposition of solid Zn(OH)$_2$ to ZnO and water is an endothermic process at room temperature, but is increasingly

favorable if larger energy is provided through higher temperature and ultrasonic treatment. Acoustic cavitation and sonochemistry accelerate the decomplexation of Zn(OH)$_2$ via reactions with ultrasonically formed radical species ($^•$OH, $^•$O$_2^−$, H$_2$O$_2$, etc.) and promote the dissociation of zinc complexes, leading to a controlled supersaturation of free metal ions at the contact with GO. The crystal growth of cone-shaped ZnO−GO NPs is determined by the thermodynamically less stable polar faces with surface dipoles, which undergo rearrangement to minimize their surface energy. The final morphology is determined via two competing processes, which are based on equilibrium (minimum in the surface energy) or kinetic growth. In ZnO−GO the kinetic growth is additionally supplied by the deposition of ZnO due to the decomplexation of Zn(OH)$_2$ and volatility of zinc carboxylates during acoustic cavitation. There is an indirect evidence from work involving etching of ZnO single crystals that indicates that carboxylates inhibit the rates of dissolution by 100-fold and tend to aid

aging and growth of crystallites.[42] This may cause the arrested growth of cone-shaped ZnO−GO NPs, which acquire the final average size <100 nm.

The size distribution histogram of ZnO and ZnO−GO NPs is shown in Figure 1C,D (more details are in the Experimental Section, and Tables S1 and S2 in the Supporting Information). The majority of ZnO has average sizes of 15.33 ± 1.84 nm (26.55% of the N total number of NPs) and 36.28 ± 1.80 nm (N ∼ 22.50%). In contrast, most of ZnO−GO has average sizes of 35.95 ± 3.03 nm (N ∼ 14.95%), 69.51 ± 3.41 nm (N ∼ 12.61%), and 15.55 ± 2.28 nm (N ∼ 12.34%), 25.01 ± 2.28 nm (N ∼ 10.36%).

The X-ray powder diffraction analysis shows the characteristic reflexes of hexagonal ZnO phase with the wurtzite structure (JCPDS 36-1451) of ZnO and ZnO−GO NPs (Figure 1E). Details about the experimental XRD data and the calculated interplanar spacing d values can be found in Table S3 (Supporting Information).

No diffraction peaks of synthesized GO (shown for comparison), $Zn(OH)_2$ (JCPDS 48-1066), graphite (amcsd 0000049) and diamond (amcsd 0013983) were observed, demonstrating that both ZnO and ZnO−GO NPs are composed of a pure ZnO crystalline phase. The size t of crystallites was calculated using the Scherrer formula (details are in the Experimental Section) with the estimated values of Δ_{θ_B} (ZnO) = 0.326 and Δ_{θ_B} (ZnO−GO) = 0.368, β (ZnO) ≈ 0.005 and β (ZnO−GO) ≈ 0.006 (Figure S1, Supporting Information). The size t of ZnO crystallites is 25.37 nm and of ZnO−GO is 22.45 nm, indicating that NPs with the cone-shaped morphology have a smaller width than nonuniform nanoparticles with random orientation.

The ζ-potential of ZnO−GO (−3.6 ± 2.3 mV) is comparable to ZnO (−4.7 ± 2.7 mV) but not to GO (−19.9 ± 5.4 mV) (Figure S2, Supporting Information). ZnO−GO is composed of Zn (∼33.5 ± 2.1) atom %, O (∼33.9 ± 1.9) atom %, and C (∼32.6 ± 1.7) atom %, as revealed from the EDX spectra (Figure S3 and Table S4, Supporting Information). For comparison, ZnO NPs contain Zn (∼42.7 ± 2.3) atom %, O (∼41.2 ± 1.9) atom %, and C (∼32.6 ± 1.7) atom % and have the atomic ratio of Zn/O as ∼1.04 similar with ZnO−GO (∼0.99).

3.2. Electronic Molecular Structure of ZnO−GO Nanoparticles. The electronic molecular structure of ZnO−GO NPs was examined by the UV−visible absorption and SERS spectroscopy methods, aiming at understanding the interaction of ZnO with GO and determining the impact of ultrasound on the formation of nanocomposites. The UV−visible absorption and SERS spectra of GO, ZnO, and ZnO−GO NPs are shown in Figure 2. The UV−visible spectrum of GO exhibits a strong absorption band with two peaks at ∼219 nm (5.66 eV) and at ∼264 nm (4.70 eV) due to the $\pi_{C=C}−\pi_{C=C}^{*}$ transitions in neighboring carbon atoms with sp^2 hybridization and those, which are bonded with oxygen in the form of carboxyl and carbonyl groups located at the edges of the graphene sheets[43] (Figure 2A).

The red shift of the second absorption peak (∼264 nm) demonstrates the reduction of the electronic structure in GO due to a decreased concentration of oxygen-containing functional groups,[44] in agreement with the ζ-potential data. The absorption spectrum of ZnO NPs shows two distinct bands at ∼210 nm (5.90 eV) and ∼369 nm (3.36 eV) on an elevated continuum, in agreement with the characteristic electronic transitions of II−VI-semiconductor clusters.[45] The
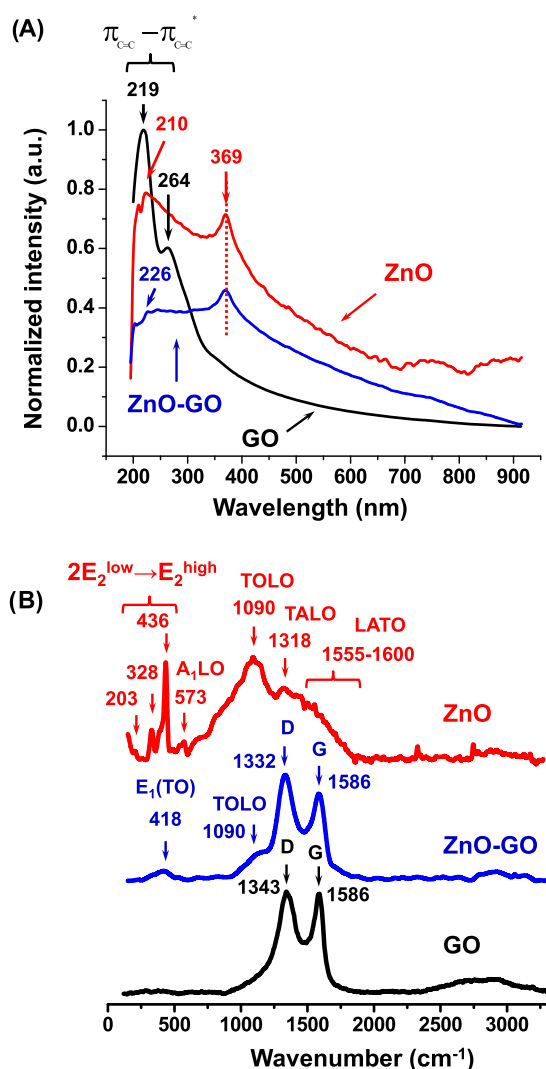

Figure 2. (A) UV−visible absorption and (B) SERS spectra (λ_{exc} = 633 nm) of GO (black line), ZnO (red line), and ZnO−GO (blue line) NPs in aqueous solutions. The vibrational bands of ZnO designated as TO, TOLO, TALO, and LATO correspond to transverse and longitudinal optical components being formed by optical overtones and combinations in ZnO.

band at ∼210 nm can be assigned to the charge transfer between ZnO clusters and the solvent band of OH^- in water.[46] The peak at ∼369 nm is the intrinsic band-gap absorption of ZnO due to the electron transitions from the valence to the conduction band ($O_{2p} \rightarrow Zn_{3d}$). This peak is indicative of ZnO NPs (<100 nm size) being formed by the Ostwald growth mechanism.

The UV−visible absorption spectrum of ZnO−GO NPs shows several small bands in the wavelength region from 226 to 312 nm and a distinct peak at ∼369 nm (Figure S4, Supporting Information). The appearance of manifold electronic transitions in the first region points out to the charge transfer in the close junction between ZnO and GO, which is inversely proportional to the adsorption strength of the anion.[47] The appearance of a distinct peak in the longer wavelength region (∼369 nm) occurs due to decreasing quantum confinement with increasing particle growth parameters such as 2D surface area and thickness. As this shift is related to the quantum size effect, the equation considering the
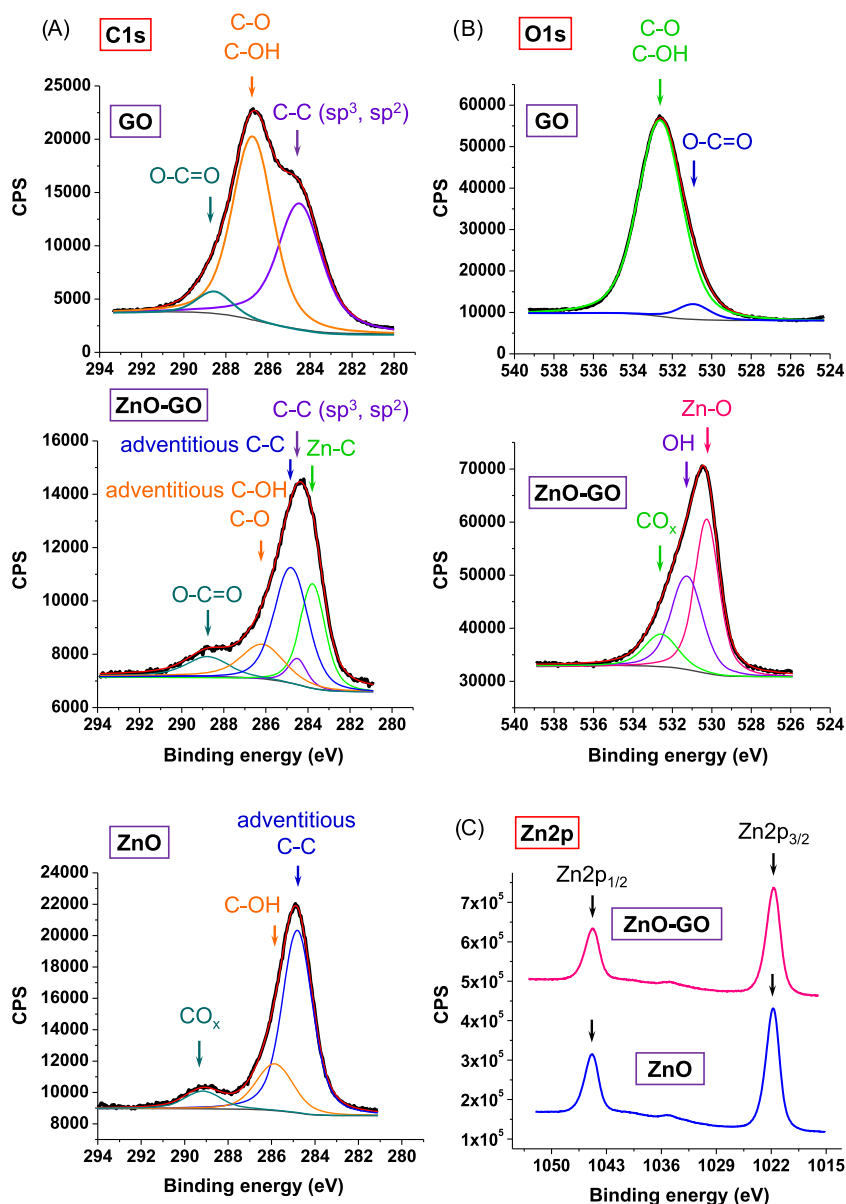
Figure 3. Representative XPS spectra of GO, ZnO, and ZnO−GO NPs showing the XPS lines of (A) C 1s, (B) O 1s, and (C) Zn 2p (CPS: counts per second). The curve fitting of the C 1s, O 1s, and Zn 2p spectra was completed using a Gaussian−Lorentzian peak shape after performing a Shirley background correction. The color coding in (A) and (B) represents raw spectra (black) and their fits (red), and fitted peak components are presented in other colors. The raw XPS Zn 2p spectra of ZnO and ZnO−GO NPs are shown in blue and pink colors, respectively.

effective mass model of the particle radius as a function of peak absorbance wavelength was applied for the estimation of ZnO nucleation centers in ZnO−GO NPs.[48] The estimated mean radius of nucleation centers is ∼2.66 nm, considering the effective mass for electrons $m_e = 0.26$ and holes $m_h = 0.59$ in ZnO.

SERS spectroscopy was applied to examine the surface structure of synthesized ZnO−GO NPs in comparison with ZnO and GO (Figure 2B). GO exhibits characteristic Raman bands at ∼1343 cm^{-1} due to the K-point phonons of A_{1g} D breathing mode and ∼1586 cm^{-1} due to the zone center phonons of E_{2g} G mode with the IntD/IntG ratio of ∼1.03, indicating that GO is composed of the hexagonal carbon structure with sp^2 hybridization.[49] SERS spectrum of ZnO NPs exhibits fundamental optical modes of wurtzite-type ZnO crystals. The most prominent Raman bands appearing as E_2 modes at ∼328 cm^{-1} ($E_2^{high} - E_2^{low}$) and ∼436 cm^{-1} E_2^{high} are

assigned to the oxygen vibration in the ZnO crystal lattice (Table S5, Supporting Information). A broad intensive Raman peak at ∼1090 cm^{-1} can be assigned to the transverse and longitudinal optical components (TO and LO) in ZnO with random orientation.

In contrast, SERS spectrum of ZnO−GO NPs shows a broad polar band at ∼418 cm^{-1} and can be assigned to E_1 TO mode with a shoulder at ∼377 cm^{-1} (A_1 TO). The decreased intensity, broadening and a blue shift of this Raman peak indicates that the mechanical action of ultrasound on ZnO with GO does not lead to the crystal lattice disorders, in agreement with the XRD analysis (more details in the Supporting Information). SERS spectrum of ZnO−GO shows strong Raman bands of GO with a blue-shifted D mode at ∼1332 cm^{-1} and a nonshifted G mode, which appears without a significant broadening. The IntD/IntG ratio is ∼1.2, demonstrating the increased disorder in GO nanosheets, which

can be caused by the formation of ZnO−GO NPs with a cone-shaped morphology.[41] In this spectrum, prominent Raman bands of ZnO do not appear in the 1090−1601 cm^{-1} frequency region, but develop a small shoulder, indicating the presence of ZnO without second-order optical components. Both the increased disorder in GO and a small peak from ZnO demonstrate that ZnO−GO formation with the cone-shaped morphology can occur without the replacement of carbon atoms in the skeleton avoiding the breakage of the graphene nanostructure.

3.3. Surface Chemical Composition of ZnO−GO Nanoparticles. The surface chemical composition and bonding of ZnO−GO NPs was studied by the X-ray photoelectron spectroscopy and compared with GO and ZnO (Figure 3). The XPS survey scans of GO (black line), ZnO (red line), and ZnO−GO (blue line) NPs were performed in a range of 1200 to 0 eV and the elements of C, O and Zn are identified (Figure S5, Supporting Information).

Next, the binding energy of C 1s lines was examined to understand the change in oxidation state and chemical environment of GO and ZnO−GO NPs (Figure 3A). The XPS C 1s line of GO shows a peak, which is fitted to three components at ∼284.5, ∼286.7, and ∼288.6 eV being assigned to carbon with sp^2 and sp^3 hybridization in aromatic C−C bonds,[50] carbon in C−O bond,[51] and O−C=O bond of the carboxyl group.[52,53] In addition, the peak at ∼286.7 eV can be indicative of the C−OH hydroxide type of carbon with the hydrogen-bridge oxide structure, in which the H atom can be symmetrically placed between two oxygen atoms.

In contrast, the XPS C 1s spectrum of ZnO−GO exhibits a peak, which is fitted to five components at ∼283.8, ∼284.5, ∼284.8, ∼286.2, and ∼288.8 eV, revealing the presence of Zn−C,[54] carbon with sp^2 and sp^3 hybridization and adventitious carbon in C−C bond,[52] carbon in C−O bonds in hydroxyl group,[55−58] and O−C=O bond of the carboxyl group.[50,52,55−58] The component at ∼283.8 eV is observed at higher binding energy values than of Zn−C being examined in the literature (e.g., ∼282.2 eV), and this chemical shift of 1.6 eV can be caused by the interaction with the carbon and oxygen atoms resulting in the changed electron density, which is transferred from zinc to oxygen atom and then to the carbon atom.

For comparison, the XPS C 1s spectrum of ZnO[59] (Figure 3A, bottom) was fitted by adventitious carbon at ∼284.8 eV, adsorbed hydroxyl groups at ∼285.9 eV[55−58] and CO$_x$ at ∼289.2 eV due to contribution of carbonate-type species or to adsorption of molecular water.[59]

The XPS O 1s line in GO is introduced by two components at ∼530.9 eV (O−C=O bonds) and ∼532.6 eV (C−OH bond)[52] (Figure 3B). In contrast to GO, both XPS O 1s lines in ZnO−GO (Figure 3B) and ZnO (Figure S6A, Supporting Information) are composed of three components: ∼530.3, ∼531.3, and ∼532.6 eV, indicating Zn−O bonding in ZnO (i.e., the O$_2^-$ ions on the wurtzite structure of the hexagonal Zn^{2+} ion array, which are surrounded by zinc atoms in close proximity to nearest-neighbor O$_2^-$ ions), O$_2^-$ ions that are in oxygen-deficient regions within the ZnO structure, and chemisorbed OH species on the ZnO surface including CO$_x$.[41,60]

Both XPS Zn 2p lines of ZnO and ZnO−GO NPs show Zn 2p$_{3/2}$ peaks at ∼1021.8 eV and Zn 2p$_{1/2}$ at ∼1044.9 eV, revealing Zn^{2+} bound to oxygen in the ZnO structure, which

was confirmed by the Zn LMM Auger lines at ∼498.2 eV (kinetic energy, ∼988.5 eV) and a shoulder at ∼495 eV (kinetic energy, ∼990 eV) (Figure S6, Supporting Information). The formation of metallic Zn is excluded because no shift to higher kinetic energy ∼992 eV was observed in Zn LMM spectra.

In our work, ZnO and ZnO−GO NPs were formed using the ultrasound-assisted hydrothermal reaction of ZnSO$_4$ and NaOH.[41] In this reaction mechanism, an excess of hydroxide is required to transform the intermediate phase of Zn(OH)$_2$ into ZnO NPs via the dissolution−precipitation process, in which the surface composition and morphology of the final product are controlled by the H$_2$O/Zn^{2+}/OH$^-$ stoichiometric mole ratio. We may assume that in ZnO−GO, the surface carboxyl (−O−C=O) groups of GO together with OH can contribute to the catalytic hydroxylation effect, which is also accelerated by ultrasound, on the transformation of Zn(OH)$_2$ to ZnO in such a way that carbon atoms are not intercalated into the ZnO wurtzite crystalline structure, which is free of impurities.

3.4. Ultrasonic Complexation of ASA with ZnO−GO Nanoparticles. The ζ-potential values of free ASA (−0.48 ± 3.73 mV), ASA−ZnO (−0.90 ± 2.59 mV), and ASA−ZnO−GO (−1.51 ± 2.36 mV) are changed toward more neutral values, indicating the complexation of ASA with ZnO and ZnO−GO compared with the data of ZnO (−4.7 ± 2.7 mV) and ZnO−GO (−3.6 ± 2.3 mV) NPs (Figure S7, Supporting Information).

The UV−visible absorption spectra of free ASA show two distinct peaks at ∼242 nm and ∼278 nm (Figure S8 and Table S6, Supporting Information), which can be assigned to salicylic acid (SA) and ASA with the C1 point group structure, in agreement with the computed sum of electronic transitions of SA. ASA−ZnO and ASA−ZnO−GO NPs exhibit a broad absorption maximum in the region 200−300 nm with a peak at ∼370 nm, which is indicative of the acetyl group with the complexed starch and ZnO/ZnO−GO (Figure S8, Supporting Information). Other absorption bands, which appear in the wavelength region 700−1100 nm, reveal the excitation of solvent molecules that are in close proximity to the surface of ASA and NPs. The Beer−Lambert law and the calculated optical density (OD) absorption values of ASA−ZnO and ASA−ZnO−GO (0.79 and 0.58, Table S6, Supporting Information) allowed for estimating the concentration of pharmaceutical substances in ASA−ZnO (∼283.5 μg/mL) and in ASA−ZnO−GO (∼208.1 μg/mL).

Next, the complexation of ASA with ZnO and ZnO−GO NPs was studied by Raman spectroscopy (Figure 4). Raman spectrum of free ASA shows its characteristic manifold vibrational modes and reveals the presence of starch (∼260, 319, 422, and 919 cm^{-1}) in a compound (Table S7, Supporting Information). Characteristic Raman bands of inactive ingredients such as talc, calcium stearate, citric acid, and SiO$_2$ were not observed (more details in the Supporting Information).

The mass fractions of ASA and starch are ∼4.21 wt % and ∼0.82 wt % in free ASA, respectively, as determined by the Raman intensity ratio method,[40] and the calculated data are presented in Table 1. In contrast, the mass fractions of ASA and starch in ASA−ZnO NPs are by 2 and 3 orders of magnitude lower than in ASA−ZnO−GO being comparable to the values in free ASA, i.e., ∼3.38 and ∼0.67 wt %. The estimated concentration of ASA in free ASA is ∼167 μmol/L, in ASA−ZnO (∼1 μmol/L) and in ASA−ZnO−GO (∼134

(A) ASA

(B) ASA-ZnO

(C) ASA-ZnO-GO

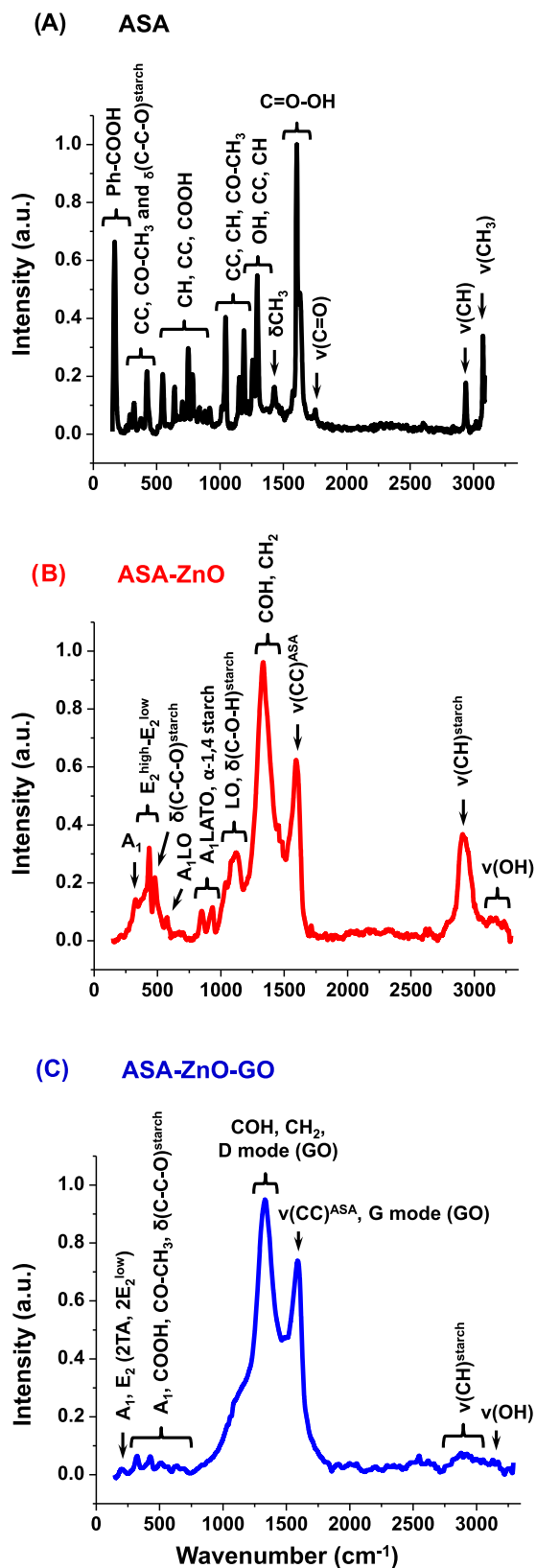**Figure 4.** Raman spectra of (A) free ASA, (B) ASA−ZnO, and (C) ASA−ZnO−GO NPs (λ_{exc} = 633 nm).

μmol/L), revealing that ASA forms a strong complex with ZnO−GO. The lowest concentration of ASA and starch in ASA−ZnO NPs in relation to free ASA and ASA−ZnO−GO can be caused by the following effects: (1) pH-dependent

swelling effect of starch during interaction with ZnO and the ionization state of carboxylic groups in aqueous solution[61] and (2) sonochemical modification of starch during acoustic cavitation. The swelling of starch in aqueous solution suggests that water can penetrate ASA−ZnO and lead to leaching of ASA. We may assume that modification of starch can be enhanced by ZnO and ultrasound, resulting in the extraction of ASA and increased solubility (hydrolysis) of starch from NPs. These effects may be retarded in ASA−ZnO−GO NPs due to the ZnO−GO structure, which forms a strong complex with ASA. It was reported that Zn^{2+} more easily interact with the hydroxyl oxygen of the starch molecular chain, leading to the hydrolysis of its glycoside bonds. As a result, weakening of the intermolecular hydrogen bonding and reduction of the crystalline regions of starch occur.[62] Zn^{2+} can appear as a result of dissolution of ZnO NPs in aqueous solution, which typically occurs under acidic conditions. In our experiments, the pH of aqueous colloidal solutions was 5.5, meaning that dissolution of ZnO is less probable. On the other hand, ultrasound can contribute to the dissolution of ZnO and release of Zn^{2+},[63] which can be retained to a higher degree in the ZnO−GO structure.

Several vibrational modes in the Raman spectrum of ASA−ZnO−GO NPs became weaker in the frequency regions <1000 and 2900–3200 cm^{-1}, while peaks at ~838, 932, 1035, and 1113 cm^{-1} disappear, which can be caused by the ultrasonic hydrolysis of starch and its stronger binding to ASA−ZnO−GO than to ASA−ZnO. The hydrolysis of starch is pronounced in ASA−ZnO NPs, in agreement with the UV−visible absorption, XPS, and Raman spectroscopy data.

ASA−ZnO and ASA−ZnO−GO NPs were synthesized by ultrasound, which forms acoustic cavitation in aqueous solution and induces sonochemical reactions. Cavitation microjets and shear forces, arising from the collapse of bubbles, can chemically functionalize starch through the interaction with free-radical species, resulting in its enhanced oxidation and swelling power, and increased porosity and solubility.[64] Sonication of starch for 3 min increases its crystallinity degree, causes the molecular scission of starch chains, and reduces its molecular weight, which acquire increased portion of highly mobile fraction as proved by ^{1}H and ^{13}C NMR spectroscopy.[65] The opened structure of starch complexed within ASA−ZnO and ASA−ZnO−GO can enhance the penetration of various chemical agents and catalysts, and significantly improve chemical reactions. Later in the text, different properties of these potential pharmaceutical nanocomposites will be demonstrated in their interaction with probiotic *E. coli* M-17 and performance of the Fenton chemical reaction.

3.5. *E. coli* M-17 Growth Inhibition by ASA−ZnO−GO Nanoparticles. The growth inhibition of probiotic *E. coli* M-17 bacteria, as a model microorganism, was assessed by interaction with free ASA, ASA−ZnO, and ASA−ZnO−GO NPs (Figure 5). Figure 5A−D shows true color photo images of *E. coli* M-17 colonies grown on differential agar media in Petri dishes without any treatment and after incubation with free ASA, ASA−ZnO, and ASA−ZnO−GO NPs. Control experiments were performed by incubating pristine differential medium alone (no bacteria) and with free ASA, ASA−ZnO, and ASA−ZnO−GO NPs at 37 °C for 20 h (Figure S9, Supporting Information): no visible bacteria or any other microorganisms were observed after incubation. In contrast, a tendency was revealed in the decreased amount of *E. coli* M-17

Table 1. Concentration and Mass Fraction of ASA and Starch in ASA−ZnO and ASA−ZnO−GO NPs Estimated by the Raman Intensity Ratio Method in Comparison with Free ASA

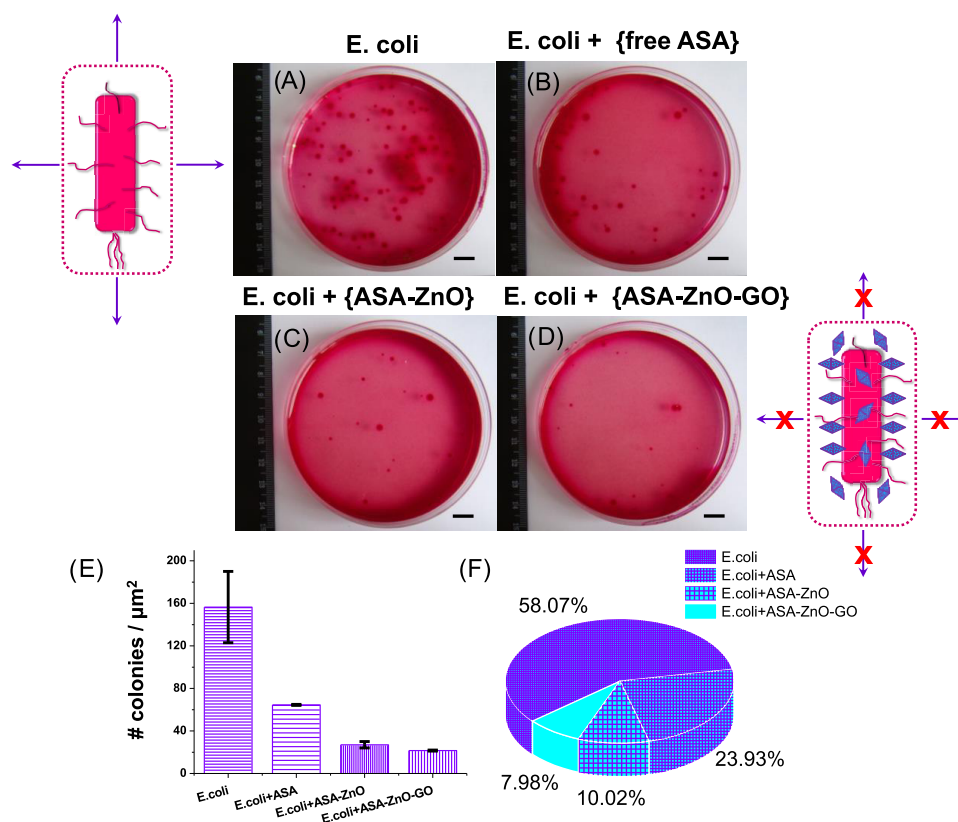| compound	α	concentration, μM		mass fraction, wt %	
		ASA	starch	ASA	starch
free ASA	18.11	167.00	43.00	4.21	0.82
ASA−ZnO	0.12	1.10	0.29	2.80×10^{-2}	5.00×10^{-3}
ASA−ZnO−GO	14.58	134.00	35.00	3.38	0.67

Figure 5. (A−D) True color photo images of live free *E. coli* M-17 without any treatment and after incubation with pristine ASA (*E. coli* + {free ASA}), ASA−ZnO (*E. coli* + {ASA−ZnO}), and ASA−ZnO−GO (*E. coli* + {ASA−ZnO−GO}). The scale bar is 1 cm. (E) The calculated statistical histogram showing the number of bacterial colonies per surface area (#/μm^2) and (F) a distribution diagram of a grown bacterial surface area relative to live free *E. coli* (in %) reveal the bacteriostatic effect of ultrasonically complexed ASA−ZnO−GO NPs in comparison to free ASA and ASA−ZnO. The error bars are the standard errors from 45 optical microscope images (more details are in the Supporting Information).

bacteria after treatment with NPs following the order from large to small: *E. coli* M-17 + {free ASA} → *E. coli* M-17 + {ASA−ZnO} → *E. coli* M-17 + {ASA−ZnO−GO} (Figure 5B−D). Details about the calculated data with their standard errors and deviation values can be found in Table S8 (Supporting Information). Overall, live *E. coli* M-17 populations occupy ∼58% of the total surface area after 20 h of incubation, which is characteristic of a fast-growing type of a bacteria family (more details in the Supporting Information).

The number of bacterial colonies per surface area decreased by 2.4 times in a sample of {*E. coli* M-17 + free ASA}, by 5.8 times in {*E. coli* M-17 + ASA−ZnO}, and by 7.3 times in {*E. coli* M-17 + ASA−ZnO−GO} (Figure 5E and Table S8), and the occupied average surface areas of grown treated *E. coli* M-17 were ∼23.9, ∼10.0, and ∼8.0% with respect to free *E. coli* M-17 (Figure 5F), demonstrating the pronounced bacteriostatic effect of ASA−ZnO and ASA−ZnO−GO NPs in comparison to free ASA.

ASA is known to be an effective antioxidant, protecting cells against $H_2O_2^-$ or O_2^- induced oxidative stress, thereby enhancing the preventive and therapeutical effects in many oxidative stress-relevant diseases. The ASA's minimum inhibitory concentration (MIC) against *E. coli* M-17 is in the range of 1.2−2.7 mg/mL, which is far above the concentration being used in this work, meaning that the motility of probiotic *E. coli* M-17 will not be completely eliminated, in agreement with our experimental data (Figure 5).

In addition, the presence of starch in free ASA can enhance the motility of *E. coli* M-17 as it was demonstrated with other probiotic bacteria (e.g., *Lactobacillus* and *Bifidobacteria*), resulting in the prevention of colon cancer.[9] The pronounced effect of starch can be ascribed to its oxidation, which increases the content of gelatinized resistant starch via transformation of its hydroxyl groups into carboxyl or carbonyl groups, breaking amylose or amylopectin chains, and changing its linkages and the bond between C_2 and C_3 (Figure S10, Supporting Information).

However, in the presence of a metal catalyst, the oxidation of starch by H_2O_2 becomes more complex involving a radical chain reaction. In this reaction, H_2O_2 is rapidly decomposed
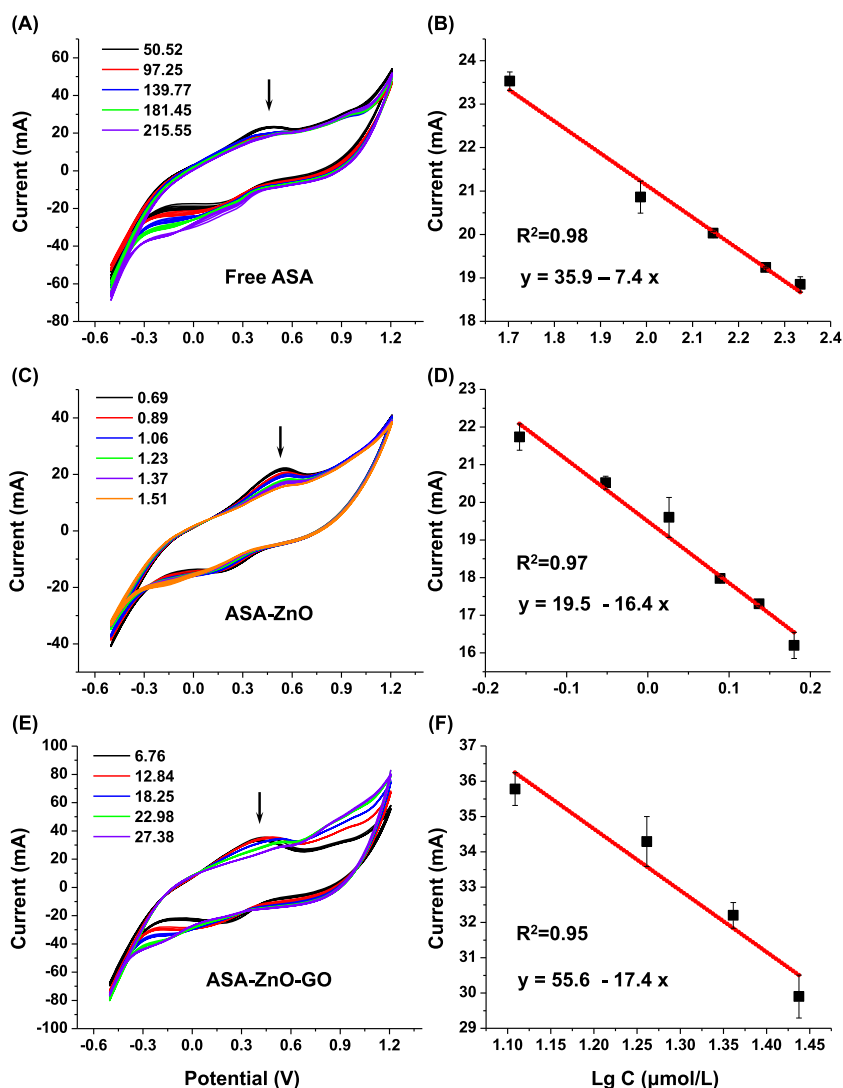
Figure 6. Relative response of current (mA) in aqueous solutions of (A) free ASA, (C) ASA−ZnO, and (E) ASA−ZnO−GO NPs recorded in an applied voltage range of −0.5 to +1.2 V by varying the amount of ASA in nanomaterials. (B, D, F) Peak values of the measured current (mA) vs concentration of ASA (μmol/L) calculated in Lg C, revealing the linear relationship $y = a - bx$, with a decrescent slope b.

into hydroxyl radicals (•OH), yielding new radicals. The carbonyl functional group is primarily produced during peroxide oxidation, followed by a smaller amount of formed carboxyl groups. In our work, ASA−ZnO and ASA−ZnO−GO NPs contain carboxyl and hydroxyl groups, suggesting the presence of strongly oxidized starch. Oxidized starch is susceptible to hydrogen-bond formation with the hydroxyl groups in amylose and amylopectin molecules, thereby enhancing the structural and tensile strength integrity to the polymeric matrix.

It was reported that ZnO NPs exhibit bactericidal activity against *E. coli* through the formation of reactive oxygen species (ROS: O_2^-, H_2O_2, singlet oxygen $^1O_2$ and •OH) and oxidative stress at MIC ∼ 5 mg/mL.[66] The released Zn^{2+} ions have been reported to be toxic to bacteria too, but eluted zinc ions cannot be considered to inhibit the bacterial growth because of the low solubility of ZnO *in vivo*. It is accepted by the community that ZnO NPs of smaller size produce a larger amount of •OH radicals and cause bacterial suicide response, which is characterized by *E. coli* growth arrest under continuous stress conditions, while maintaining the metabolism in bacteria.[67] •OH radicals can be formed as a result of reaction between

O_2^- and H_2O_2, and can be catalyzed by ZnO because its surface is coated by OH. O_2^- can capture H^+ in solution, yielding the formation of hydroperoxyl radical $HO_2^•$, which can penetrate the cellular membrane like H_2O_2, causing its damage and disorganization in the cell wall, thereby inhibiting the growth of the cells or leading to their apoptosis. It is proposed that H_2O_2 is one of the primary factors in the bacteriostatic effect caused by ZnO NPs.[68]

The interaction with the cellular membrane of *E. coli* M-17 can be modulated with ASA−ZnO−GO NPs due to the enhanced biocompatibility of GO and FDA-approved ZnO. It was reported that GO can cause no viability loss, at a concentration of 50 μg/mL, indicating the low toxicity of GO to HeLa cells and enabling long-term antibacterial performance.[69] We may consider that GO cuts the *E. coli* M-17 membrane because these effects were previously observed at a low concentration of GO colloidal suspension (<6 μg/mL).[17] Moreover, sharp edges of cone-shaped ASA−ZnO−GO NPs can enable a tighter contact and complexation with the bacterial cellular membrane, thereby enhancing the bacteriostatic effects of *E. coli* M-17.

3.6. Antioxidant Efficiency of ASA−ZnO−GO Nanoparticles. Next, we performed the electrochemical Fenton reaction process with free ASA, ASA−ZnO, and ASA−ZnO−GO NPs to find out the scavenging efficiency of hydroxyl radicals by these potential pharmaceutical nanomaterials. The cyclic voltammograms of the relative response of current (mA) vs the applied voltage (from −0.5 to +1.2 V) by varying the concentration of pharmaceutics in free ASA, ASA−ZnO, and ASA−ZnO−GO NPs are shown in Figure 6.

Control electrochemical experiments were performed in aqueous solutions containing Fe^{2+} cations (catalyst) and sodium phosphate dibasic (phosphate-buffered solution, pH 9) before and after reaction with hydrogen peroxide under similar conditions, confirming that the Fenton process took place only after addition of hydrogen peroxide, which is accompanied by the appearance of two characteristic redox peaks at ∼0.29 V (∼14.57 mA) and ∼0.15 V (∼8.56 mA) (Figure S11, Supporting Information), in agreement with the literature considering different types of phosphate buffer solutions. In addition, the electrochemical measurement of fresh aqueous solution of free ASA (pH 3) was also performed as another control experiment, demonstrating the prevailed reduction of ASA due to the appearance of the larger peak at ∼0.83 V (∼33.15 mA) and a negligible one at ∼0.53 V (∼4.74 mA) caused by oxidation (Figure S12, Supporting Information).

Cyclic voltammograms of free ASA during the electro-Fenton process show a characteristic current peak of hydroxyl radicals at ∼0.48 V (∼23.54 mA) due to oxidation and a small broad peak at ∼0.09 V (ca. −20.88 mA) due to reduction only at a smaller concentration of ASA (∼60.62 μmol/L) (Figure 6A). As the concentration of ASA increased up to ∼217 μmol/L, the oxidation peak disappeared, and two reduction peaks were developed at increased the current peak values at ∼0.15 V (ca. −24.35 mA) and ∼0.83 V (ca. −3.24 mA), indicating that free ASA neutralizes •OH radicals during oxidation and enhances the reduction processes. The decrease of the current peak values of hydroxyl radicals follows the linear relationship at the increased concentration of ASA, and its rate is ∼7.4 as determined from the slope (Figure 6B).

In contrast, cyclic voltammograms of ASA−ZnO NPs show a pronounced current peak of •OH radicals at ∼0.55 V (∼21.74 mA) due to oxidation and a peak at ∼0.24 V (ca. −13.67 mA) due to reduction at the smallest concentration of ASA (∼0.69 μmol/L), demonstrating the enhanced activity of redox reactions due to the conjugation of ASA and ZnO (Figure 6C). Both peaks are significantly decreased at an increased concentration of ASA−ZnO with the oxidation peak values at ∼0.59 V (∼16.20 mA), while the reduction peak disappeared at the highest available amount of ASA (∼1.51 μmol/L), indicating that ASA−ZnO nanoparticles diminish •OH radicals as well as the reduction processes. This is also evidenced from the lower current peak edge values (at ∼1.51 μmol/L) at ca. −31.76 mA (−0.50 V) and ∼38.53 mA (1.20 V) with respect to the initial edge values (at ∼0.69 μmol/L) at ca. −41.31 mA (−0.5 V) and ∼41.38 mA (1.20 V). Similar to free ASA, the decreased current peak values of hydroxyl radicals also follow the linear relationship, but at a higher rate of ∼16.4, demonstrating that the redox reactions are accelerated by ASA−ZnO during the electro-Fenton process (Figure 6D).

Similarly to ASA, cyclic voltammograms of ASA−ZnO−GO NPs show a current peak of hydroxyl radicals at ∼0.47 V

(∼35.78 mA) due to oxidation and a small broad peak at ∼0.18 V (ca. −25.51 mA) due to reduction only at the smallest available concentration (∼6.76 μmol/L) (Figure 6E). These current peak values are larger than those in free ASA, pointing out to the higher electron density of ASA−ZnO−GO NPs. At an increased concentration of ASA−ZnO−GO (∼27.38 μmol/L), the oxidation peak disappeared like in free ASA, and only one reduction peak was developed at ∼0.71 V (ca. −11.85 mA) with significantly increased current edge peak values at −75.43 mA (−0.50 V) and ∼84.81 mA (1.20 V) being higher than in free ASA (−68.12 and 52.01 mA), demonstrating more efficient neutralization of •OH radicals during oxidation by ASA−ZnO−GO. Similar to free ASA and ASA−ZnO, the decrease of current peak values of hydroxyl radicals follows the linear relationship with the increased concentration of ASA−ZnO−GO, but at a higher rate of ∼17.4, demonstrating the pronounced antioxidant efficiency of ASA−ZnO−GO in acceleration of redox reactions in the electro-Fenton process.

4. CONCLUSIONS

A new single-step ultrasonic method (20 kHz) is demonstrated for the formation of ZnO−GO NPs with the average size of <70 nm. ZnO−GO are composed of the pure crystalline ZnO wurtzite phase and have a cone-shaped morphology with the Zn/O atomic ratio ∼1.0. The surface structure of ZnO−GO contains hydroxyl and carboxylate groups that are particularly useful for the ultrasonic complexation with pristine ASA.

Ultrasonically complexed ASA−ZnO−GO NPs more effectively inhibit the growth of probiotic *E. coli* M-17 bacteria than free ASA or ASA−ZnO. This improved bacteriostatic function of ASA−ZnO−GO can be attributed to the complexation of ASA and starch with ZnO−GO, biocompatibility due to GO and ZnO. Moreover, ASA−ZnO−GO NPs more efficiently neutralize •OH radicals during the electro-Fenton process than free ASA or ASA−ZnO at the concentration of ∼28 μmol/L, which is lower than 100 μmol/L and can be considered as biosafe and nontoxic to eukaryotic cells according to FDA rules.

This new knowledge substantially enriches our understanding about the improvement of pharmaceutical function of ASA, especially its antioxidant property, and discloses the important roles of ZnO and GO in contact-dependent growth modulation of probiotic *E. coli* M-17 bacteria. These new findings can be particularly useful for the fundamental studies of the drug−enzyme, drug−metal, and drug−biological cell interactions, and can be expanded to other drugs in the treatment of gastrointestinal tract diseases, diabetes, and cancer.

■ ASSOCIATED CONTENT

Ⓢ Supporting Information

The Supporting Information is available free of charge at https://pubs.acs.org/doi/10.1021/acsanm.0c03111.

> Synthesis of graphene oxide (GO); size estimation of nanoparticles using the statistical method of electron microscopy; X-ray powder diffraction analysis of nanoparticles; ζ-potential plots of nanoparticles; energy-dispersive X-ray fluorescence spectral analysis of nanoparticles; UV−visible absorption spectrum of ZnO−GO nanoparticles in the wavelength region from 200 to 500 nm; experimental data obtained from SERS spectra of nanoparticles; X-ray photoelectron survey scans of

nanoparticles, XPS O 1s spectrum of ZnO and XPS Zn LMM spectra of ZnO and ZnO−GO nanoparticles; UV−visible absorption spectra and their analysis of aqueous solutions of free ASA, ZnO and ZnO−GO nanoparticles, ASA−ZnO, and ASA−ZnO−GO nanoparticles in comparison to free ASA after 3 min of sonication; Raman spectra of free ASA and ultrasonically formed ASA−ZnO and ASA−ZnO−GO nanoparticles (λ_{exc} = 633 nm); control experiments with *E. coli* M-17 bacteria; chemical structures of free ASA, potato starch, and GO; and control experiments (electro-Fenton process) (PDF)

AUTHOR INFORMATION

Corresponding Author

Darya Radziuk − *Laboratory of Integrated Micro- and Nanosystems, Belarusian State University of Informatics and Radioelectronics, 220013 Minsk, Republic of Belarus;* ● orcid.org/0000-0001-7287-4303; Email: radziuk@bsuir.by

Authors

Anastasia Tkach − *Laboratory of Integrated Micro- and Nanosystems, Belarusian State University of Informatics and Radioelectronics, 220013 Minsk, Republic of Belarus*

Aliaksandr Burko − *Laboratory of Applied Plasmonics, Belarusian State University of Informatics and Radioelectronics, 220013 Minsk, Republic of Belarus*

Hanna Bandarenka − *Laboratory of Applied Plasmonics, Belarusian State University of Informatics and Radioelectronics, 220013 Minsk, Republic of Belarus; Polytechnic School, Arizona State University, Mesa, Arizona 85212, United States*

Tatyana Khrustaleva − *Laboratory of Applied Plasmonics, Belarusian State University of Informatics and Radioelectronics, 220013 Minsk, Republic of Belarus; Biochemistry Group of Multidisciplinary Diagnostic Laboratory, Institute of Physiology, National Academy of Sciences of Belarus, 220072 Minsk, Republic of Belarus*

Dmitry Zhigulin − *Scientific-Technical Center "Belmicrosystems", 220108 Minsk, Republic of Belarus*

Ljudmila Tabulina − *Laboratory of Integrated Micro- and Nanosystems, Belarusian State University of Informatics and Radioelectronics, 220013 Minsk, Republic of Belarus*

Vladimir Labunov − *Laboratory of Integrated Micro- and Nanosystems, Belarusian State University of Informatics and Radioelectronics, 220013 Minsk, Republic of Belarus*

Kateřina Veltruská − *Department of Surface and Plasma Science, Charles University, 18000 Prague 8, Czech Republic*

Vladimír Matolín − *Department of Surface and Plasma Science, Charles University, 18000 Prague 8, Czech Republic*

Complete contact information is available at:
https://pubs.acs.org/10.1021/acsanm.0c03111

Author Contributions

The manuscript was written through contributions of all authors. All authors have given approval to the final version of the manuscript.

Notes

The authors declare no competing financial interest.

REFERENCES

(1) Sonnenborn, U. *Escherichia coli* Strain Nissle 1917—from Bench to Bedside and Back: History of a Special *Escherichia coli* Strain with Probiotic Properties. *FEMS Microbiol. Lett.* **2016**, *363*, No. fnw212.

(2) Ahumada-Santos, Y. P.; Báez-Flores, M. E.; Díaz-Camacho, S. P.; Uribe-Beltrán, M. deJ.; Eslava-Campos, C. A.; Parra-Unda, J. R.; Delgado-Vargas, F. Association of Phylogenetic Distribution and Presence of Integrons with Multidrug Resistance in *Escherichia coli* Clinical Isolates from Children with Diarrhoea. *J Infect. Public Health* **2020**, *13*, 767−772.

(3) Fitzpatrick, L. R.; Small, J.; Hoerr, R. A.; Bostwick, E. F.; Maines, L.; Koltun, W. A. In Vitro and in Vivo Effects of the Probiotic *Escherichia coli* Strain M-17: Immunomodulation and Attenuation of Murine Colitis. *Br. J Nutr.* **2008**, *100*, 530−541.

(4) von Wright, A. Regulating the Safety of Probiotics—The European Approach. *Curr. Pharm. Des.* **2005**, *11*, 17−23.

(5) Shelkovaia, N. G.; Kupchinskiĭ, L. G.; Znamenskiĭ, V. A.; Bondarenko, V. M. An Electron Microscopic Study of the Interaction of Bacterial Intestinal Microflora and Rotavirus Virions. *Zh. Mikrobiol., Epidemiol. Immunobiol.* **1991**, *9*, 18−21.

(6) Bukharin, O. V.; Perunova, N. B.; Ivanova, E. Y.; Andryuschenko, S. V. Intermicrobial Discrimination in Pair of Probiotic Strains of *E. coli* M-17 and *E. coli* LEGM-18. *Zh. Mikrobiol., Epidemiol. Immunobiol.* **2016**, *3*, 3−9.

(7) Vakhitov, T. I.; Protasov, E. A.; Visnol'd, N. V.; Tolparov, I. T.; Petrov, L. N. Isolation and Identification of Growth Stimulators of *Escherichia coli* M-17. *Zh. Mikrobiol., Epidemiol. Immunobiol.* **2003**, *2*, 7−12.

(8) Adler, S. N. The Probiotic Agent *Escherichia coli* M-17 has a Healing Effect in Patients with IBS with Proximal Inflammation of the Small Bowel. *Dig. Liver Dis.* **2006**, *38*, 713.

(9) Zimmermann, P.; Curtisa, N. Antimicrobial Effects of Antipyretics. *Antimicrob. Agents Chemother.* **2017**, *61*, No. e02268-16.

(10) Jian, Z.; Tang, L.; Yi, X.; Liu, B.; Zhang, Q.; Zhu, G.; Wang, G.; Gao, T.; Li, C. Aspirin Induces Nrf2-mediated Transcriptional Activation of Haem Oxygenase-1 in Protection of Human Melanocytes from H_2O_2-induced Oxidative Stress. *J. Cell. Mol. Med.* **2016**, *20*, 1307−1318.

(11) Chen, H.; Fang, Q.; Tu, Q.; Liu, C.; Yin, J.; Yin, Y.; Xia, L.; Bian, X.; Zhang, Y. Identification of a Contact-dependent Growth Inhibition System in the Probiotic *Escherichia coli* Nissle 1917. *FEMS Microbiol. Lett.* **2018**, *365*, No. e1002877.

(12) Cha, S.-H.; Hong, J.; McGuffie, M.; Yeom, B.; VanEpps, J. S.; Kotov, N. A. Shape-Dependent Biomimetic Inhibition of Enzyme by Nanoparticles and Their Antibacterial Activity. *ACS Nano* **2015**, *9*, 9097−9105.

(13) Hu, C.; Wang, L.-L.; Lin, Y.-Q.; Liang, H.-M.; Zhou, S.-Y.; Zheng, F.; Feng, X.-L.; Rui, Y.-Y.; Shao, L.-Q. Nanoparticles for the

Treatment of Oral Biofilms: Current State, Mechanisms, Influencing Factors, and Prospects. *Adv. Healthcare Mater.* **2019**, No. 1901301.

(14) Mi, G.; Shi, D.; Wang, M.; Webster, T. J. Reducing Bacterial Infections and Biofilm Formation using Nanoparticles and Nano-structured Antibacterial Surfaces. *Adv. Healthcare Mater.* **2018**, No. 1800103.

(15) U.S. Food and Drug Administration. *Code of Federal Regulations Title 21*; 21CFR182.8991; FDA, April 1, 2019.

(16) Wang, Y.-W.; Cao, A.; Jiang, Y.; Zhang, X.; Liu, J.-H.; Liu, Y.; Wang, H. Superior Antibacterial Activity of Zinc Oxide/Graphene Oxide Composites Originating from High Zinc Concentration Localized around Bacteria. *ACS Appl. Mater. Interfaces* **2014**, *6*, 2791−2798.

(17) Martín, C.; Kostarelos, K.; Prato, M.; Bianco, A. Biocompatibility and Biodegradability of 2D Materials: Graphene and Beyond. *Chem. Commun.* **2019**, *55*, 5540−5546.

(18) Yadav, R. S.; Pandey, A. C. Needle-like ZnO Nanostructure Synthesized by Organic-Free Hydrothermal Process. *Phys. E* **2008**, *40*, 660−663.

(19) Zare, M.; Namratha, K.; Byrappa, K.; Surendra, D. M.; Yallappa, S.; Hungund, B. Surfactant Assisted Solvothermal Synthesis of ZnO Nanoparticles and Study of Their Antimicrobial and Antioxidant Properties. *J Mater. Sci. Technol.* **2018**, *34*, 1035−1043.

(20) Widiyastuti, W.; Wang, W.-N.; Purwanto, A.; Lenggoro, I. W.; Okuyama, K. A Pulse Combustion-Spray Pyrolysis Process for the Preparation of Nano- and Submicrometer-Sized Oxide Particles. *J. Am. Ceram. Soc.* **2007**, *90*, 3779−3785.

(21) Saloga, P. E. J.; Thünemann, A. F. Microwave-Assisted Synthesis of Ultrasmall Zinc Oxide Nanoparticles. *Langmuir* **2019**, *35*, 12469−12482.

(22) Hinman, J. J.; Suslick, K. S. Nanostructured Materials Synthesis Using Ultrasound. *Top Curr. Chem.* **2017**, *375*, 59−94.

(23) Zhong, L.; Liu, H.; Samal, M.; Yun, K. Synthesis of ZnO Nanoparticles-decorated Spindle-shaped Graphene Oxide for Application in Synergistic Antibacterial Activity. *J. Photochem. Photobiol., B* **2018**, *183*, 293−301.

(24) Mitra, P.; Dutta, D.; Das, S.; Basu, T.; Pramanik, A.; Patra, A. Antibacterial and Photocatalytic Properties of ZnO-9-Aminoacridine Hydrochloride Hydrate Drug Nanoconjugates. *ACS Omega* **2018**, *3*, 7962−7970.

(25) Zhao, W.; Wei, J.-S.; Zhang, P.; Chen, J.; Kong, J.-L.; Sun, L.-H.; Xiong, H.-M.; Möhwald, H. Self-Assembled ZnO Nanoparticle Capsules for Carrying and Delivering Isotretinoin to Cancer Cells. *ACS Appl. Mater. Interfaces* **2017**, *9*, 18474−18481.

(26) Ye, D.-X.; Ma, Y.-Y.; Zhao, W.; Cao, H.-M.; Kong, J.-L.; Xiong, H.-M.; Möhwald, H. ZnO-Based Nanoplatforms for Labeling and Treatment of Mouse Tumors without Detectable Toxic Side Effects. *ACS Nano* **2016**, *10*, 4294−4300.

(27) Akbarian, M.; Mahjoub, S.; Elahi, S. M.; Zabihi, E.; Tashakkorian, H. Green Synthesis, Formulation and Biological Evaluation of a Novel ZnO Nanocarrier Loaded with Paclitaxel as Drug Delivery System on MCF-7 Cell Line. *Colloids Surf., B* **2020**, *186*, No. 110686.

(28) Sadhukhan, P.; Kundu, M.; Rana, S.; Kumar, R.; Das, J.; Sil, P. C. Microwave Induced Synthesis of ZnO Nanorods and Their Efficacy as a Drug Carrier with Profound Anticancer and Antibacterial Properties. *Toxicol. Rep.* **2019**, *6*, 176−185.

(29) Mocanu, A.; Isopencu, G.; Busuioc, C.; Popa, O.-M.; Dietrich, P.; Socaciu-Siebert, L. Bacterial Cellulose Films with ZnO Nanoparticles and Propolis Extracts: Synergistic Antimicrobial Effect. *Sci. Rep.* **2019**, *9*, No. 17687.

(30) Laurenti, M.; Lamberti, A.; Genchi, G. G.; Roppolo, I.; Canavese, G.; Vitale-Brovarone, C.; Ciofani, G.; Cauda, V. Graphene Oxide Finely Tunes the Bioactivity and Drug Delivery of Mesoporous ZnO Scaffolds. *ACS Appl. Mater. Interfaces* **2019**, *11*, 449−456.

(31) Alipour, N.; Namazi, H. Chelating ZnO-dopamine on the Surface of Graphene Oxide and its Application as pH-responsive and Antibacterial Nanohybrid Delivery Agent for Doxorubicin. *Mater. Sci. Eng., C* **2020**, *108*, No. 110459.

(32) Radziuk, D.; Mikhnavets, L.; Vorokhta, M.; Matolín, V.; Tabulina, L.; Labunov, V. Sonochemical Formation of Copper/Iron-modified Graphene Oxide Nanocomposites for Ketorolac Delivery. *Chem. - Eur. J* **2019**, *25*, 6233−6245.

(33) Fiadosenka, U.; Matsukovich, A.; Tabulina, L.; Labunov, V.; Radziuk, D. The Properties of the Sonochemically Functionalized Nonsteroidal Anti-inflammatory Drug Ketorolac in Fe₃O₄-Graphene Oxide Nanocomposite. *New J. Chem.* **2019**, *41*, 16118−16122.

(34) Tkach, A.; Matsukovich, A.; Krekoten, N.; Tabulina, L.; Labunov, V.; Radziuk, D. Graphene Oxide-Coated CuO Nanoparticles for Functionalization of Acetylsalicylic Acid and Diclofenac. *ACS Appl. Nano Mater.* **2020**, *3*, 5593−5604.

(35) Tkach, A.; Fiadosenka, U.; Burko, A.; Bandarenka, H. V.; Matsukovich, A.; Krekoten, N.; Tabulina, L.; Labunov, V.; Radziuk, D. Polyvinyl Alcohol Enhances Acetylation of Ascorbic Acid in Superparamagnetic-Graphene Oxide Nanoparticles Ultrasonically Complexed with Acetylsalicylic Acid. *ACS Appl. Polym. Mater.* **2020**, *2*, 3663−3673.

(36) Marcano, D. C.; Kosynkin, D. V.; Berlin, J. M.; Sinitskii, A.; Sun, Z.; Slesarev, A.; Alemany, L. B.; Lu, W.; Tour, J. M. Improved Synthesis of Graphene Oxide. *ACS Nano* **2010**, *4*, 4806−4814.

(37) Edwards, L. J. The Dissolution and Diffusion of Aspirin in Aqueous Media. *Trans. Faraday Soc.* **1951**, *47*, 1191−1210.

(38) Margulis, M. A.; Margulis, I. M. Calorimetric Method for Measurement of Acoustic Power Absorbed in a Volume of a Liquid. *Ultrason. Sonochem.* **2003**, *10*, 343−345.

(39) Zavatski, S.; Khinevich, S. N.; Girel, K.; Redko, S.; Kovalchuk, N.; Komissarov, I.; Lukashevich, V.; Semak, I.; Mamatkulov, K.; Vorobyeva, M.; Arzumanyan, G.; Bandarenka, H. Surface Enhanced Raman Spectroscopy of Lactoferrin Adsorbed on Silvered Porous Silicon Covered with Graphene. *Biosensors* **2019**, *9*, 34−119.

(40) Kontoyannis, C. G.; Orkouf, M. Quantitative Non-destructive Determination of Salicylic Acid Acetate in Aspirin Tablets by Raman Spectroscopy. *Talanta* **1994**, *41*, 1981−1984.

(41) Moezzi, A.; Cortie, M.; McDonagh, A. Aqueous Pathways for the Formation of Zinc Oxide Nanoparticles. *Dalton Trans.* **2011**, *40*, 4871−4878.

(42) Govender, K.; Boyle, D. S.; Kenway, P. B.; O'Brien, P. Understanding the Factors that Govern the Deposition and Morphology of Thin Films of ZnO from Aqueous Solution. *J. Mater. Chem.* **2004**, *14*, 2575−2591.

(43) Eda, G.; Lin, Y.-Y.; Mattevi, C.; Yamaguchi, H.; Chen, H.-A.; Chen, I.-S.; Chen, C.-W.; Chhowalla, M. Blue Photoluminescence from Chemically Derived Graphene Oxide. *Adv. Mater.* **2010**, *22*, 505−509.

(44) Neogi, A.; Karna, S.; Shah, R.; Phillipose, U.; Perez, J.; Shimada, R.; Wang, Z. M. Surface Plasmon Enhancement of Broadband Photoluminescence Emission from Graphene Oxide. *Nanoscale* **2014**, *6*, 11310−11315.

(45) Spanhel, L. Colloidal ZnO Nanostructures and Functional Coatings: A Survey. *J. Sol-Gel Sci. Technol.* **2006**, *39*, 7−24.

(46) Wood, A.; Giersig, M.; Hilgendorff, M.; Vilas-Campos, A.; Liz-Marzán, L. M.; Mulvaney, P. Size Effects in ZnO: the Cluster to Quantum Dot Transition. *Aust. J Chem.* **2003**, *56*, 1051−1057.

(47) Ludi, B.; Niederberger, M. Zinc Oxide Nanoparticles: Chemical Mechanisms and Classical and Non-classical Crystallization. *Dalton Trans.* **2013**, *42*, 12554−12568.

(48) Pesika, N. S.; Stebe, K. J.; Searson, P. C. Determination of the Particle Size Distribution of Quantum Nanocrystals from Absorbance Spectra. *Adv. Mater.* **2003**, *15*, 1289−1291.

(49) Ferrari, A. C. Raman Spectroscopy of Graphene and Graphite: Disorder, Electron-phonon Coupling, Doping and Nonadiabatic Effects. *Solid State Commun.* **2007**, *143*, 47−57.

(50) Yang, D.; Velamakannia, A.; Bozoklu, G.; Park, S.; Stoller, M.; Piner, R. D.; Stankovich, S.; Jung, I.; Field, D. A.; Ventrice, C. A., Jr.; Ruoff, R. S. Chemical Analysis of Graphene Oxide Films after Heat and Chemical Treatments by X-ray Photoelectron and Micro-Raman Spectroscopy. *Carbon* **2009**, *47*, 145−152.

(51) Stankovich, S.; Dikin, D. A.; Piner, R. D.; Kohlhaas, K. A.; Kleinhammes, A.; Jia, Y.; Wu, Y.; Nguyen, S. T.; Ruoff, R. S. Synthesis of Graphene-based Nanosheets via Chemical Reduction of Exfoliated Graphite Oxide. *Carbon* **2007**, *45*, 1558−1565.

(52) Al-Gaashania, R.; Najjarc, A.; Zakariaa, Y.; Mansoura, S.; Atieh, M. A. XPS and Structural Studies of High Quality Graphene Oxide and Reduced Graphene Oxide Prepared by Different Chemical Oxidation Methods. *Ceram. Int.* **2019**, *45*, 14439−14448.

(53) Johra, F. T.; Lee, J.-W.; Jung, W.-G. Facile and Safe Graphene Preparation on Solution based Platform. *J. Ind. Eng. Chem.* **2014**, *20*, 2883−2887.

(54) Alshammari, A. S.; Chi, L.; Chen, X.; Bagabas, A.; Kramer, D.; Alromaeh, A.; Jiang, Z. Visible-light Photocatalysis on C-doped ZnO Derived from Polymer-assisted Pyrolysis. *RSC Adv.* **2015**, *5*, 27690−27698.

(55) Araújo, M. P.; Soares, O. S. G. P.; Fernandes, A. J. S.; Pereira, M. F. R.; Freire, C. Tuning the Surface Chemistry of Graphene Flakes: New Strategies for Selective Oxidation. *RSC Adv.* **2017**, *7*, 14290−14301.

(56) Ganguly, A.; Sharma, S.; Papakonstantinou, P.; Hamilton, J. Probing the Thermal Deoxygenation of Graphene Oxide Using High-resolution in Situ X-ray-based Spectroscopies. *J. Phys. Chem. C* **2011**, *115*, 17009−17019.

(57) López-Díaz, D.; Holgado, M.; García-Fierro, J. L.; Velázquez, M. M. Evolution of the Raman Spectrum with the Chemical Composition of Graphene Oxide. *J. Phys. Chem. C* **2017**, *121*, 20489−20497.

(58) Barreca, D.; Gasparotto, A.; Maccato, C.; Maragno, C.; Tondello, E. ZnO Nanoplatelets Obtained by Chemical Vapor Deposition, Studied by XPS. *Surf. Sci. Spectra* **2007**, *14*, 19−26.

(59) Ballerini, G.; Ogle, K.; Barthes-Labrousse, M.-G. The Acid−Base Properties of the Surface of Native Zinc Oxide Layers: an XPS Study of Adsorption of 1, 2-diaminoethane. *Appl. Surf. Sci.* **2007**, *253*, 6860−6867.

(60) Hsieh, P.-T.; Chen, Y.-C.; Kao, K.-S.; Wang, C.-M. Luminescence Mechanism of ZnO Thin Film Investigated by XPS Measurement. *Appl. Phys. A* **2007**, *90*, 317−321.

(61) Namazi, H.; Hasani, M.; Yadollahi, M. Antibacterial Oxidized Starch/ZnO Nanocomposite Hydrogel: Synthesis and Evaluation of Its Swelling Behaviours in Various pHs and Salt Solutions. *Int. J. Biol. Macromol.* **2019**, *126*, 578−584.

(62) Ma, J.; Zhu, W.; Tian, Y.; Wang, Z. Preparation of Zinc Oxide-Starch Nanocomposite and Its Application on Coating. *Nanoscale Res. Lett.* **2016**, *11*, 200.

(63) Tso, C.; Zhung, C.; Shih, Y.; Tseng, Y.-M.; Wu, S.; Doong, R. Stability of Metal Oxide Nanoparticles in Aqueous Solutions. *Water Sci. Technol.* **2010**, *61*, 127−133.

(64) Sujka, M.; Jamroz, J. Ultrasound-treated Starch: SEM and TEM Imaging, and Functional Behaviour. *Food Hydrocolloids* **2013**, *31*, 413−419.

(65) Zhu, F. Impact of Ultrasound on Structure, Physicochemical Properties, Modifications, and Applications of Starch. *Trends Food Sci. Technol.* **2015**, *43*, 1−17.

(66) Salat, M.; Petkova, P.; Hoyo, J.; Perelshtein, I.; Gedanken, A.; Tzanov, T. Sonochemical Coating of Textiles with Hybrid ZnO/Chitosan Antimicrobial Nanoparticles. *Carbohydr. Polym.* **2018**, *189*, 198−203.

(67) Aldsworth, T. G.; Sharman, R. L. Bacterial Suicide through Stress. *Cell. Mol. Life Sci.* **1999**, *56*, 378−383.

(68) Yamamoto, O.; Hotta, M.; Sawai, J.; Sasamoto, T.; Kojima, H. Influence of Powder Characteristic of ZnO on Antibacterial Activity. *J. Ceram. Soc. Jpn.* **1998**, *106*, 1007−1011.

(69) Wang, Y.-W.; Cao, A.; Jiang, Y.; Zhang, X.; Liu, J.-H.; Liu, Y.; Wang, H. Superior Antibacterial Activity of Zinc Oxide/Graphene Oxide Composites Originating from High Zinc Concentration Localized around Bacteria. *ACS Appl. Mater. Interfaces* **2014**, *6*, 2791−2798.